



# Synthesis and enhanced electrochemical performance of $\text{LiNi}_{0.5}\text{Mn}_{1.5}\text{O}_4$ cathode materials under the assistance of polyvinylpyrrolidone

Yaqiang Lang<sup>1,2,3</sup> · Xianli Sun<sup>1,2,3</sup> · Gang Xue<sup>1</sup> · Xinhui Duan<sup>1,3</sup> · Li Wang<sup>1,2,3</sup> · Guangchuan Liang<sup>1,2,3</sup>

Received: 14 June 2022 / Revised: 31 August 2022 / Accepted: 4 September 2022 / Published online: 15 September 2022  
© The Author(s), under exclusive licence to Springer-Verlag GmbH Germany, part of Springer Nature 2022

## Abstract

$\text{LiNi}_{0.5}\text{Mn}_{1.5}\text{O}_4$  materials with hierarchical microsphere structure are prepared by PVP-assisted coprecipitation-hydrothermal method followed by high-temperature calcination. Effects of PVP molecular weights on the structure, morphology, and electrochemical properties of  $\text{LiNi}_{0.5}\text{Mn}_{1.5}\text{O}_4$  are investigated. It is found that PVP addition improves the crystallinity and disordering degree of  $\text{LiNi}_{0.5}\text{Mn}_{1.5}\text{O}_4$ . PVP molecular weights exert great influence on the particle morphology. With the increase of molecular weight, primary particle size gradually decreases and secondary particle distribution becomes more uniform. Compared with LNMO-PVP<sub>M</sub> and LNMO-PVP<sub>H</sub>, LNMO-PVP<sub>L</sub> particle possesses extra {110} surface besides {111} and {100} surfaces. Electrochemical results show that PVP addition enhances the electrochemical performance of  $\text{LiNi}_{0.5}\text{Mn}_{1.5}\text{O}_4$ , due to higher crystallinity, higher cation disordering degree, smaller primary particle size, and more uniform secondary particle distribution. LNMO-PVP<sub>L</sub> material exhibits the optimal electrochemical performance, due to extra {110} exposed surface and higher disordering degree, as well as relatively large primary particle size and slightly severe agglomerate structure.

**Keywords**  $\text{LiNi}_{0.5}\text{Mn}_{1.5}\text{O}_4$  · Polyvinylpyrrolidone · Coprecipitation-hydrothermal method · Hierarchical microsphere structure · Electrochemical performance

## Introduction

Lithium-ion batteries (LIBs) with higher energy density are urgently needed to meet the continuous development of electric vehicles (EVs) and plug-in hybrid electric vehicles (PHEVs). The energy density of LIBs is generally dependent on cathode material, which is mainly determined by the discharge capacity and operating voltage. Among them,  $\text{LiNi}_{0.5}\text{Mn}_{1.5}\text{O}_4$  (LNMO) spinel is regarded as one promising

cathode material due to high operating voltage (~4.7 V vs.  $\text{Li/Li}^+$ ), high energy density ( $650 \text{ Wh kg}^{-1}$ ), 3-D  $\text{Li}^+$  ion diffusion channel, and environmental friendliness [1, 2]. Unfortunately, the most critical issues preventing the commercial application of LNMO in power LIBs are the rapid capacity degradation during cell operation and the decomposition of electrolyte and concurrent degradation reactions at the cathode/electrolyte interface under high voltage [3, 4]. Many approaches, such as element doping [5], surface coating [6], and morphology control [7], have been applied to improve the electrochemical properties of LNMO material.

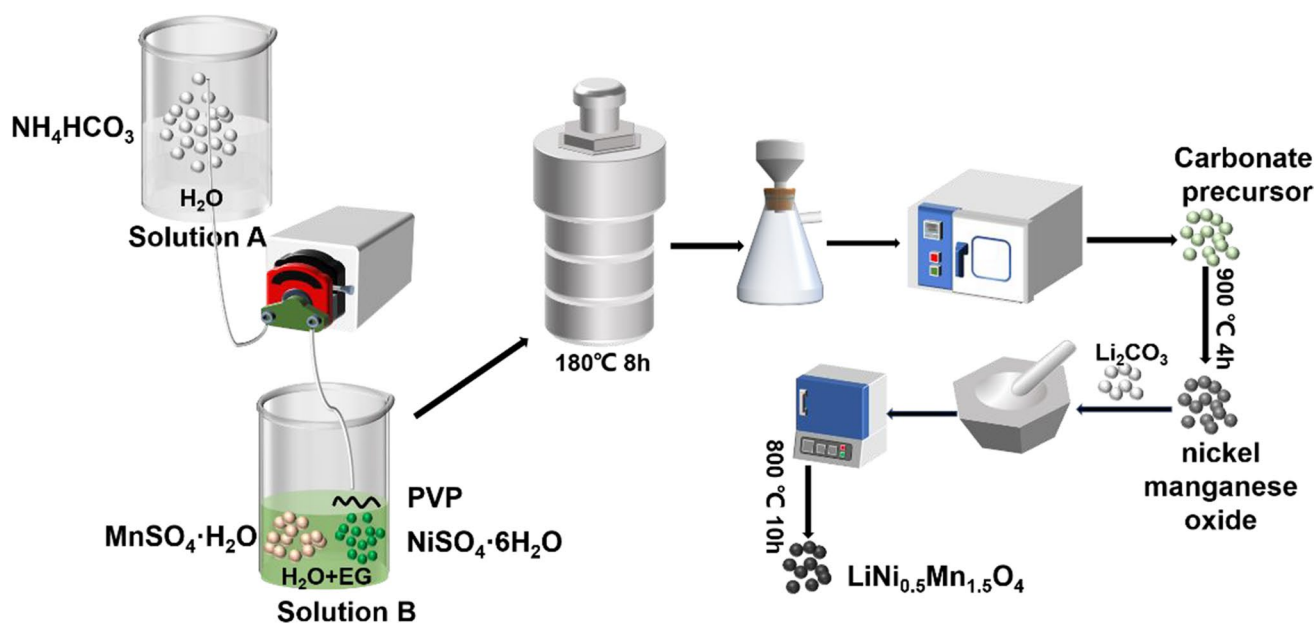
Herein, a combined coprecipitation-hydrothermal method was adopted to synthesize nickel manganese carbonate precursor, which was pre-fired, mixed with lithium source and finally calcinated at high temperature to obtain LNMO product. As for this route, the morphology of LNMO material can be regulated by changing the precursor's morphology. It is well known that surfactants can effectively tailor particle shape and size in the synthesis process [8–14]. Surfactants can be roughly divided into ionic surfactants (including cationic and anionic surfactants) and non-ionic surfactants. As

✉ Li Wang  
wangli\_hebut@163.com

<sup>1</sup> School of Materials Science and Engineering, Hebei University of Technology, Tianjin 300130, China

<sup>2</sup> Key Laboratory of Special Functional Materials for Ecological Environment and Information, Ministry of Education, Hebei University of Technology), Tianjin 300130, China

<sup>3</sup> Key Laboratory for New Type of Functional Materials in Hebei Province, Hebei University of Technology, Tianjin 300130, China



**Scheme 1** Preparation process of  $\text{LiNi}_{0.5}\text{Mn}_{1.5}\text{O}_4$  samples

a typical non-ionic surfactant, polyvinylpyrrolidone (PVP) has an alkyl hydrophobic side group and a hydrophilic pyrrolidone group, and can be easily soluble in water and many organic solvents due to the formation of hydrogen bonds between carbonyl group ( $\text{C}=\text{O}$ ) in PVP and solvent, leading to its extensive application in the synthesis of nanoparticles as a stabilizer and dispersant [15]. For example, Lin et al. [9] synthesized uniform nanosized LNMO material by adding PVP to the sol–gel process of precursor, and found that the material synthesized with PVP exhibited better electrochemical performance than that without PVP. Tian et al. [13] synthesized three  $\text{Li}_{1.2}\text{Mn}_{0.54}\text{Ni}_{0.13}\text{Co}_{0.13}\text{O}_2$  samples (LLMO-PVP, LLMO-PEG, LLMO-PVA) via coprecipitation method by using PVP, polyethylene glycol (PEG), and polyvinyl alcohol (PVA) as polymer templates, respectively, and found that LLMO-PVP exhibited the optimal electrochemical performance. Xiang et al. [14] obtained  $\text{Li}[\text{Li}_{0.131}\text{Ni}_{0.304}\text{Mn}_{0.565}]\text{O}_2$  material with uniform particle size by adding PVP and ethylene glycol (EG) in the coprecipitation process of precursor followed by high-temperature calcination, and found that the resulting material delivered excellent cycling stability and rate performance.

However, up to now, the application of PVP in the synthesis of electrode material is mostly focused on single molecular weight PVP [14] or different addition amounts [16]. It is known that PVP possesses a wide range of molecular weights, which determines the length of hydrophobic carbon chains, therefore regulating the microstructure of inorganic nanomaterials [17]. Therefore, in this work, series of  $\text{LiNi}_{0.5}\text{Mn}_{1.5}\text{O}_4$  materials with hierarchical microsphere structure were synthesized by PVP-assisted

coprecipitation-hydrothermal method followed by high-temperature calcination process. PVP with three molecular weights (average Mw: 10,000/58,000/1,300,000) were added in the coprecipitation process, and the effects of PVP molecular weights on the structure, morphology, and electrochemical properties of  $\text{LiNi}_{0.5}\text{Mn}_{1.5}\text{O}_4$  cathode materials were elaborately investigated.

## Experimental

### Sample synthesis

Scheme 1 illustrates the preparation process of  $\text{LiNi}_{0.5}\text{Mn}_{1.5}\text{O}_4$  samples. A coprecipitation-hydrothermal method was adopted to synthesize nickel manganese carbonate precursor. To be specific, solution A was prepared by dissolving 300 mmol  $\text{NH}_4\text{HCO}_3$  in 200 mL deionized water, and solution B was prepared by dissolving 15 mmol  $\text{NiSO}_4\cdot 6\text{H}_2\text{O}$ , 45 mmol  $\text{MnSO}_4\cdot \text{H}_2\text{O}$ , and 1.084 g polyvinylpyrrolidone (PVP) in a mixture of 100 mL ethylene glycol (EG) and 200 mL deionized water, where PVP with three molecular weights (average Mw: 10,000/58,000/1,300,000) were used. Then, solution A was dripped into solution B at a rate of  $6\text{ mL s}^{-1}$  by micro peristaltic pump under constant magnetic stirring. After reaction for 1 h, the resultant suspension was transferred to Teflon-lined stainless steel autoclave and heated at  $180\text{ }^\circ\text{C}$  for 8 h in an oven. After natural cooling, the precipitate was filtered, washed, and dried to get nickel manganese carbonate precursor. The precursors synthesized with three molecular weights of PVP were names

as NMC-PVP<sub>L</sub> (average Mw: 10,000), NMC-PVP<sub>M</sub> (average Mw: 58,000), and NMC-PVP<sub>H</sub> (average Mw: 1,300,000), respectively. As a control sample, the precursor without PVP was also synthesized following the same route, and labeled as NMC. The above four carbonate precursors were pre-fired at 900 °C for 4 h, then mixed with 5 wt.% excess Li<sub>2</sub>CO<sub>3</sub>, and finally calcinated at 800 °C for 10 h in air atmosphere to achieve LiNi<sub>0.5</sub>Mn<sub>1.5</sub>O<sub>4</sub> products, which were denoted as LNMO-PVP<sub>L</sub>, LNMO-PVP<sub>M</sub>, LNMO-PVP<sub>H</sub> and LNMO, respectively.

## Sample characterization

The structure of the prepared materials was analyzed with powder X-ray diffraction (XRD) using D8-FOCUS diffractometer with CuK $\alpha$  X-ray source in 2 $\theta$  range of 10–80° and Bruker V80 Fourier Transform Infrared Spectroscopy (FT-IR) in wavenumber range of 700–400 cm<sup>-1</sup>. The morphology of the materials was analyzed with Nova Nano SEM450 scanning electron microscopy (SEM) and JEOL JEM 2100F transmission electron microscope (TEM).

## Electrochemical tests

The cathode was fabricated by mixing 80 wt.% active material, 10 wt.% polyvinylidene fluoride (PVDF) and 10 wt.% Super P in N-Methyl pyrrolidone (NMP), and magnetically stirring to achieve a uniform slurry, which was casted onto Al foil with a doctor blade, and dried at 100 °C in a vacuum oven until complete evaporation of NMP. The coated Al foil was punched into round sheets with diameter of 12 mm, and the active material loading amount is ~5 mg cm<sup>-2</sup>. The cathode sheet was assembled into CR2430 coin cell in Ar-filled glove box with lithium metal anode, Celgard 2400 separator, and 1 M LiPF<sub>6</sub>-dimethyl carbonate (DMC) + ethylene carbonate (EC) + ethyl methyl carbonate (EMC) (volume ratio 1:1:1) electrolyte. The constant-current charge/discharge tests were carried out on Land CT2001A battery test system in the voltage range of 3.5–4.95 V at 25 °C.

Cyclic voltammetry (CV) test was performed on Chenhua CHI660E electrochemical workstation in the voltage range of 3.4–5.0 V. Electrochemical impedance spectroscopy (EIS) test was carried out on electrochemical workstation in the frequency range of 100 kHz to 0.01 Hz with an AC amplitude of 5 mV. Two electrode system using lithium metal as counter electrode was used in CV and EIS tests.

After 200 cycles at 1 C and 25 °C, the cathodes were extracted from the fully discharged cells, washed with dimethyl carbonate (DMC) three times, and dried overnight in the glove box. SEM and energy dispersive X-ray spectroscopy (EDS) were performed to characterize the surface morphology and surface film composition of cycled cathodes.

## Results and discussion

### Structural and morphology analysis

XRD patterns of carbonate precursors synthesized without and with different molecular weights of PVP are shown in Fig. 1a. It can be seen that all major diffraction peaks can be assigned to MnCO<sub>3</sub> with R-3C space group (JCPDS card No. 44–1472). Besides, several weak diffraction peaks of NiCO<sub>3</sub> (JCPDS card No. 12–0771) also exist, which implies that all precursors are a mixture of MnCO<sub>3</sub> and NiCO<sub>3</sub>, whereas NiCO<sub>3</sub> diffraction peaks of the precursors with PVP are weaker than those without PVP, suggesting the coprecipitation of Ni<sup>2+</sup> and Mn<sup>2+</sup> ions into single carbonate solid solution under the assistance of PVP, which is beneficial to the electrochemical performance of LiNi<sub>0.5</sub>Mn<sub>1.5</sub>O<sub>4</sub> material.

Figure 1b shows the XRD patterns of LiNi<sub>0.5</sub>Mn<sub>1.5</sub>O<sub>4</sub> samples synthesized without and with different molecular weights of PVP. All diffraction peaks can be assigned to cubic LiNi<sub>0.5</sub>Mn<sub>1.5</sub>O<sub>4</sub> spinel with *Fd3m* space group (JCPDS Card No. 80–2162), indicating that the crystal structure of LiNi<sub>0.5</sub>Mn<sub>1.5</sub>O<sub>4</sub> is not altered after PVP addition. In addition, the absence of impurities and high phase purity is believed to be favorable to the electrochemical performance

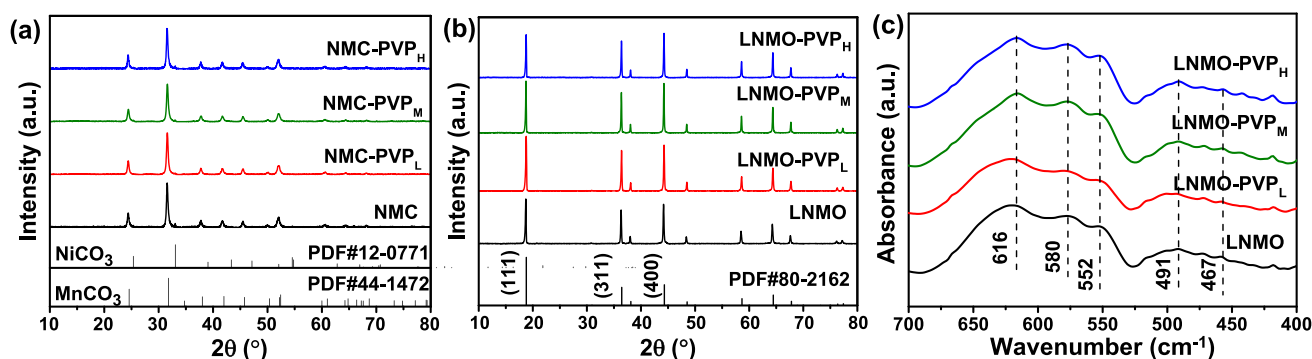


Fig. 1 XRD patterns of carbonate precursors (a), LiNi<sub>0.5</sub>Mn<sub>1.5</sub>O<sub>4</sub> samples (b), and FT-IR spectra of LiNi<sub>0.5</sub>Mn<sub>1.5</sub>O<sub>4</sub> samples (c)

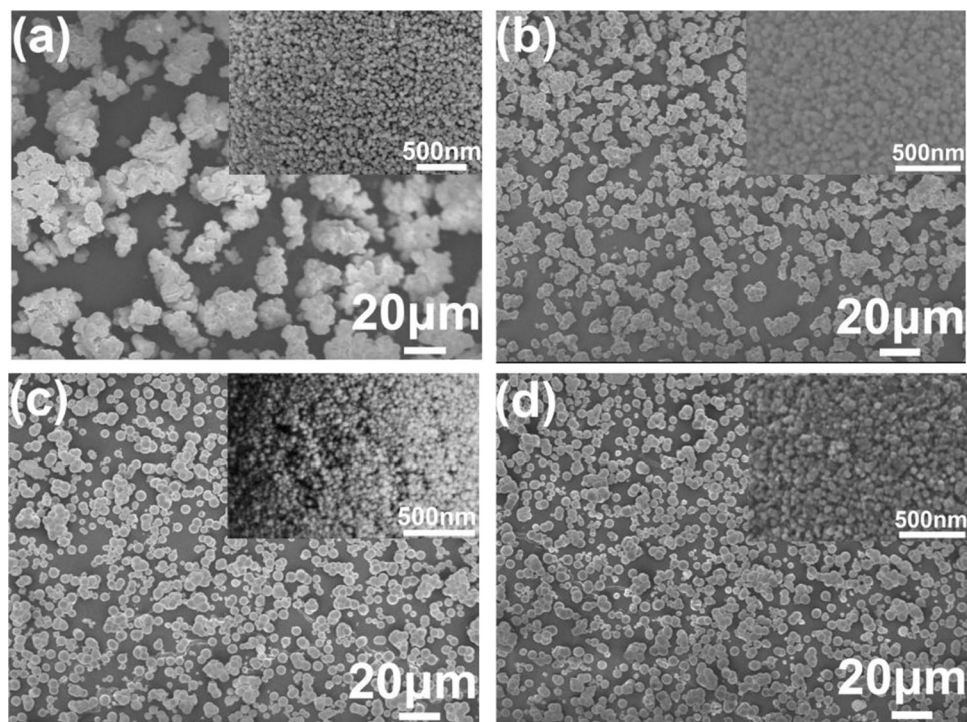
of  $\text{LiNi}_{0.5}\text{Mn}_{1.5}\text{O}_4$  material. Furthermore, the diffraction peaks of  $\text{LiNi}_{0.5}\text{Mn}_{1.5}\text{O}_4$  samples with PVP are sharper and narrower than that without PVP, meaning the enhanced crystallinity after PVP addition, which is also beneficial to the electrochemical performance of  $\text{LiNi}_{0.5}\text{Mn}_{1.5}\text{O}_4$  material. XRD patterns are refined by MDI Jade6.5 software, and the resulting lattice constants  $a$  of LNMO, LNMO-PVP<sub>L</sub>, LNMO-PVP<sub>M</sub>, and LNMO-PVP<sub>H</sub> samples are 8.1574 Å, 8.1768 Å, 8.1594 Å, and 8.1648 Å, respectively. Since  $\text{Mn}^{4+}$  has a smaller ionic radius (0.53 Å) than  $\text{Mn}^{3+}$  (0.645 Å, high spin), the varying lattice constants are supposed to be caused by differing  $\text{Mn}^{3+}$  contents [18]. As previously reported [19], inhomogeneous atom migration, which is closely connected with the structure of precursor particles, results in the generation of  $\text{Mn}^{3+}$  ions, and smaller particle size and more porous structure generally leads to shorter atom migration distance, thus resulting in the formation of less  $\text{Mn}^{3+}$  ions. Therefore, the relatively large primary particle size of NMC-PVP<sub>L</sub> precursor, as shown in the inset images of Fig. 2a–d, leads to the formation of more  $\text{Mn}^{3+}$  ions and then larger lattice constant of LNMO-PVP<sub>L</sub> than other samples. The peak intensity ratio of (311) to (400),  $I_{311}/I_{400}$ , can index the degree of tetragonal distortion from cubic spinel structure, and then the structural integrity of  $\text{LiNi}_{0.5}\text{Mn}_{1.5}\text{O}_4$  material [20]. Higher structural integrity and enhanced cycle stability is often associated with higher  $I_{311}/I_{400}$  ratio [21]. According to Fig. 1b, the  $I_{311}/I_{400}$  peak intensity ratios are 0.830, 0.906, 0.895, and 0.832, respectively, for LNMO, LNMO-PVP<sub>L</sub>, LNMO-PVP<sub>M</sub>, and LNMO-PVP<sub>H</sub> samples. In other words,

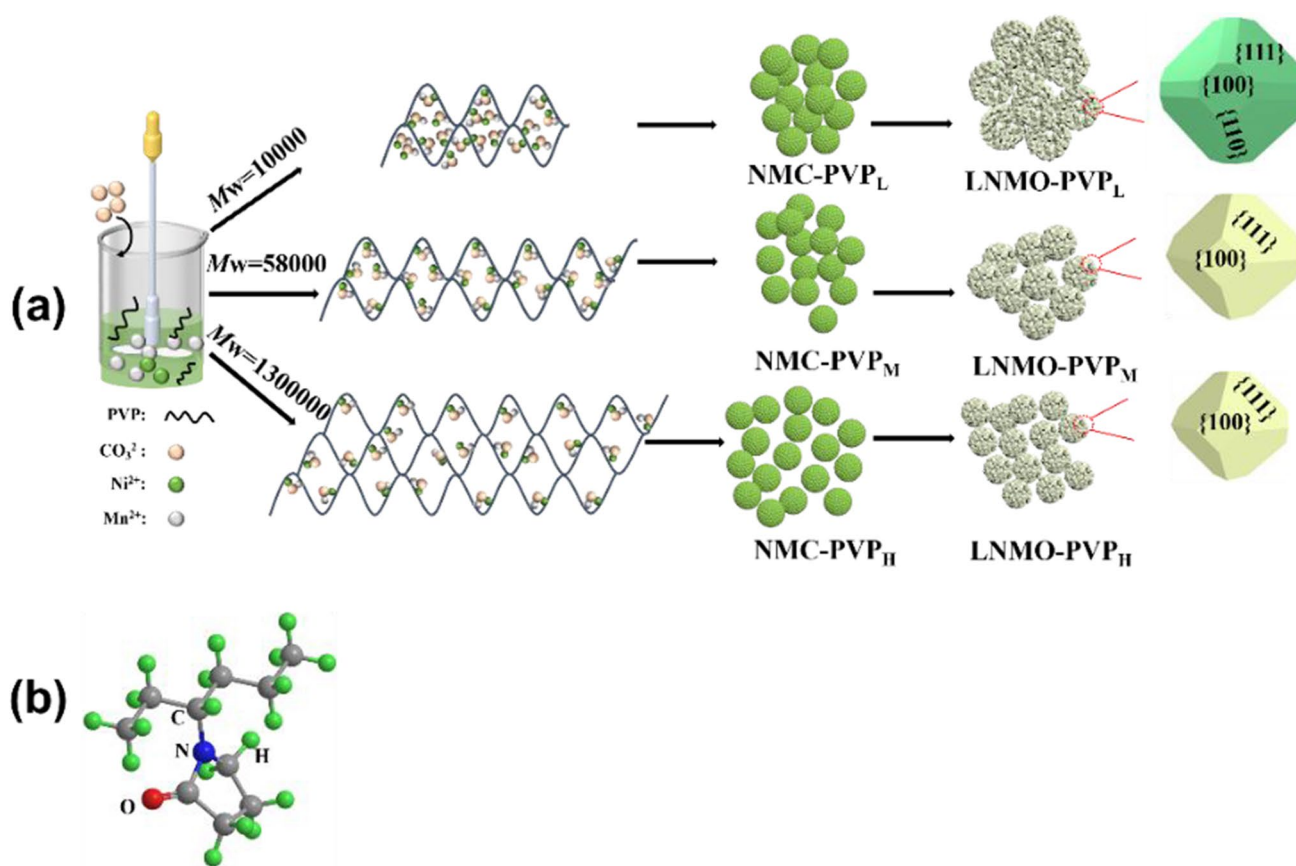
$\text{LiNi}_{0.5}\text{Mn}_{1.5}\text{O}_4$  samples with PVP have higher  $I_{311}/I_{400}$  ratios than pristine LNMO, heralding the improved structural integrity and cycling performance, as shown in Fig. 5c.

FT-IR is considered an effective means to discriminate  $P4_332$  ordered structure and  $Fd3m$  disordered structure for  $\text{LiNi}_{0.5}\text{Mn}_{1.5}\text{O}_4$  material, and the obtained FT-IR spectra are shown in Fig. 1c. It can be seen that all samples display five broadened absorption bands at 616, 580, 552, 491, and 467  $\text{cm}^{-1}$ , suggesting the major  $Fd3m$  disordered structure [22, 23]. Besides, the stronger band at 616  $\text{cm}^{-1}$  than at 580  $\text{cm}^{-1}$  is also a fingerprint of  $Fd3m$  disordered structure [21]. The  $I_{616}/I_{580}$  intensity ratios for LNMO, LNMO-PVP<sub>L</sub>, LNMO-PVP<sub>M</sub>, and LNMO-PVP<sub>H</sub> are 1.121, 1.318, 1.138, and 1.143, respectively. As widely accepted, higher intensity ratio of  $I_{616}/I_{580}$  always means higher cation disordering degree [24]. Therefore, the cation disordering degree is enhanced after PVP addition, which increases in the order of LNMO, LNMO-PVP<sub>M</sub>, LNMO-PVP<sub>H</sub>, and LNMO-PVP<sub>L</sub>. High  $\text{Mn}^{3+}$  content is always associated with high disordering degree [25], thereby  $\text{Mn}^{3+}$  content increases in the same order, in line with the results calculated based on discharge curves in Fig. 5a and the variation of lattice constants in Fig. 1c.

Figure 2a–d show SEM images of carbonate precursors synthesized without and with different molecular weights of PVP. It can be seen from Fig. 2a that pristine NMC precursor exhibits secondary irregular flake particles with severe agglomeration, due to the random growth of crystals and the agglomeration of crystal nuclei nearby, whereas all three

**Fig. 2** SEM images of carbonate precursors synthesized without and with different weights of PVP: **a** NMC, **b** NMC-PVP<sub>L</sub>, **c** NMC-PVP<sub>M</sub>, **d** NMC-PVP<sub>H</sub>





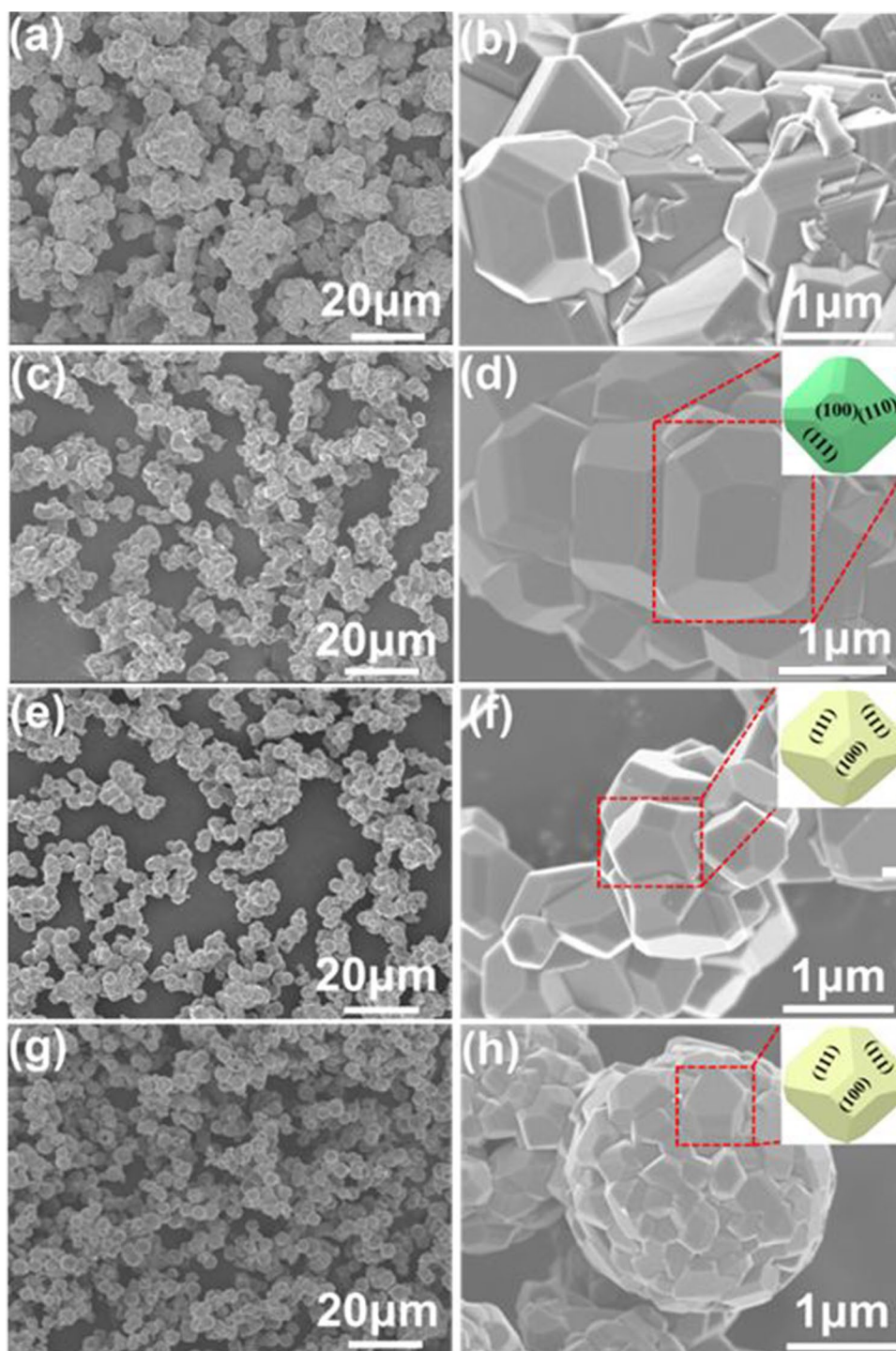
**Scheme 2** Schematic formation process of carbonate precursor and  $\text{LiNi}_{0.5}\text{Mn}_{1.5}\text{O}_4$  samples synthesized with different molecular weights of PVP (a) and molecular structure of PVP (b)

precursors synthesized with PVP display secondary microsphere particles with homogeneous distribution and less aggregation. Herein, the mass content of PVP in the solution is 9.27%, very close to 10%; therefore, PVP molecules can adsorb particles in the solution to form a more thermodynamically stable sphere [26, 27], thus leading to the formation of microsphere particles. In addition, the homogeneous distribution of secondary particles may be attributed to the molecular structure of PVP. As shown in Scheme 2(b), PVP has a pyrrolidone group in its long carbon chain, and can be well dispersed in the solution to form a homogeneous network. The network can restrict the growth of precursor and assemble the primary particles into secondary ones with homogeneous distribution. As the molecular weight of PVP increases, the longer carbon chain leads to the formation of more networks and then the generation of more dispersed secondary particles. This phenomenon is in good agreement with the finding of Izu et al. [28]. The formation process of carbonate precursor with addition of different molecular weights of PVP is illustrated in Scheme 2(a).

Figure 3a–h show SEM images of  $\text{LiNi}_{0.5}\text{Mn}_{1.5}\text{O}_4$  samples synthesized without and with different molecular

weights of PVP. It can be noticed that the particle morphology of carbonate precursors is basically inherited by  $\text{LiNi}_{0.5}\text{Mn}_{1.5}\text{O}_4$  samples. LNMO sample displays irregular particle morphology with inhomogeneous particle size and severe agglomeration, whereas the samples synthesized with three molecular weights of PVP exhibit uniformly distributed hierarchical microsphere agglomerates made up of truncated octahedral primary particles with well-developed surfaces. With the increase of PVP molecular weight, the secondary particle's dispersion degree is increased and the agglomeration degree is decreased; that is, the secondary particle distribution becomes more uniform with the molecular weight of PVP. On the other hand, the molecular weights of PVP have a marked impact on the primary particle size, which shows a gradual decreasing trend with the molecular weights of PVP. The smaller primary particle size means shorter  $\text{Li}^+$  ions diffusion distance, which is advantageous to the rate capability of  $\text{LiNi}_{0.5}\text{Mn}_{1.5}\text{O}_4$  material, as evidenced by the following rate capability result in Fig. 5b. In addition, from Fig. 3d, f, h, it is interesting to find that although the primary particles of  $\text{LNMO-PVP}_L$ ,  $\text{LNMO-PVP}_M$ ,  $\text{LNMO-PVP}_H$  all exhibit truncated octahedral shape,

**Fig. 3** SEM images of  $\text{LiNi}_{0.5}\text{Mn}_{1.5}\text{O}_4$  samples synthesized without and with different molecular weights of PVP: **a, b** LNMO, **c, d** LNMO-PVP<sub>L</sub>, **e, f** LNMO-PVP<sub>M</sub>, **g, h** LNMO-PVP<sub>H</sub>



there exist some discrepancies. The exposed surface planes were labeled in the inset of Fig. 3d, f, h based on the built characteristics of truncated octahedral  $\text{LiNi}_{0.5}\text{Mn}_{1.5}\text{O}_4$  with f.c.c structure along with previous literatures [4, 29]. Most primary particles of LNMO-PVP<sub>M</sub> and LNMO-PVP<sub>H</sub> possess {100} and {111} surfaces. Among the three main surfaces of {110}, {100}, and {111}, the surface energy increases in the order of {111}, {100}, and {110} [29]. The

lowest surface energy of {111} plane leads to the typical octahedral particle morphology of  $\text{LiNi}_{0.5}\text{Mn}_{1.5}\text{O}_4$  material [30]. However, calcination temperature higher than 800 °C could induce the appearance of {100} plane with higher surface energy, thus resulting in the formation of truncated octahedral particle [31]. In contrast, LNMO-PVP<sub>L</sub> primary particle possesses extra {110} surfaces besides {100} and {111} surfaces, presumably induced by its relatively larger

primary particle size compared with LNMO-PVP<sub>M</sub> and LNMO-PVP<sub>H</sub>. The formation process is also illustrated in Scheme 2(a).

The microstructure of LNMO-PVP<sub>L</sub> sample was further observed by TEM. From Fig. 4a, we can observe the truncated octahedral shape of LNMO-PVP<sub>L</sub> particle.

From Fig. 4b–d, we can observe distinct lattice fringes, indicating good crystallinity of the sample. The lattice fringe widths are measured to be 0.259 nm, 0.209 nm and 0.236 nm, corresponding to (311), (400) and (220) crystal planes, respectively, in good consistence with above SEM observation.

Fig. 4 TEM images of LNMO-PVP<sub>L</sub> sample

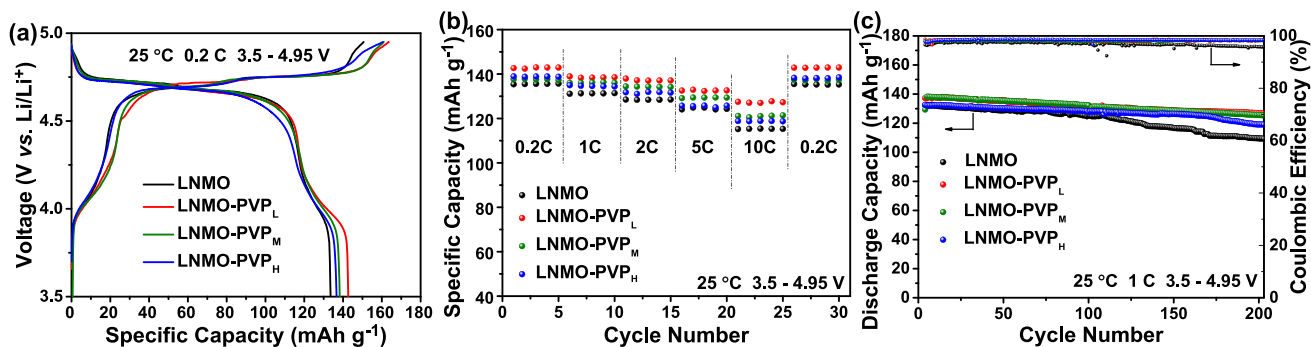
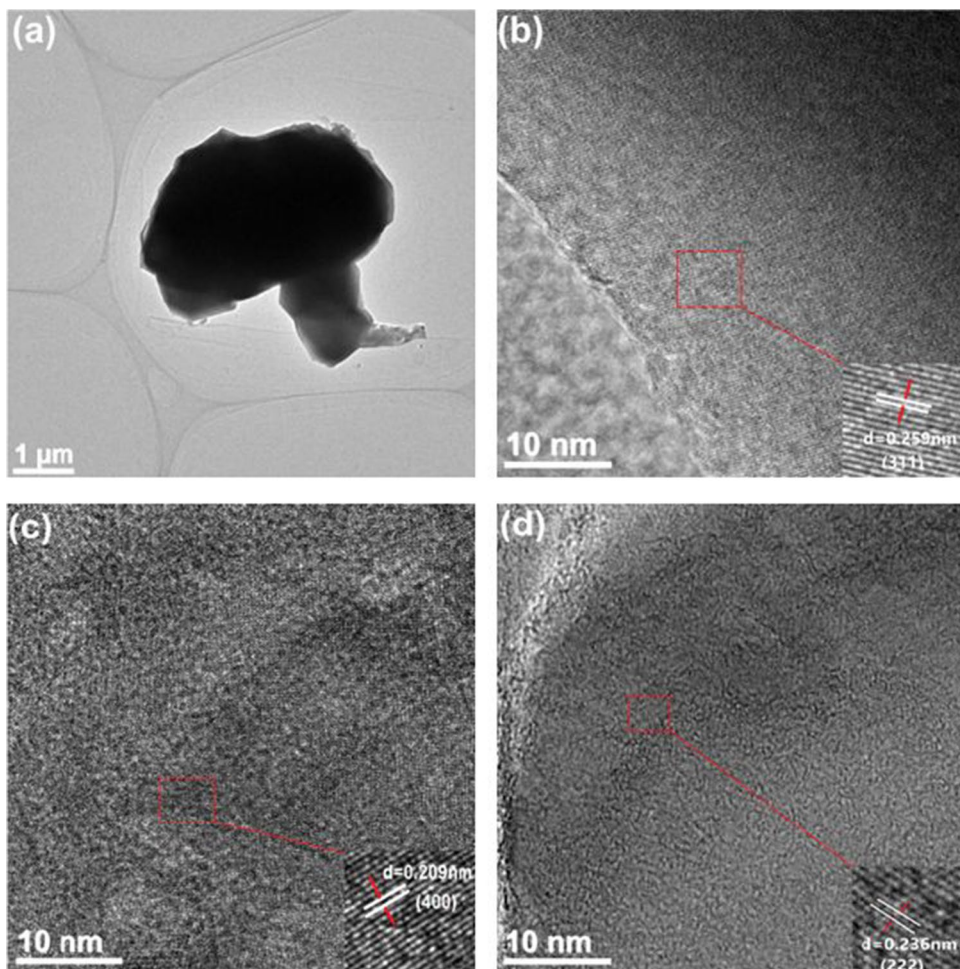


Fig. 5 Initial charge/discharge curves at 0.2 C rate (a), rate capability curves (b), and cycling performance and coulombic efficiency curves at 1 C rate (c) for LiNi<sub>0.5</sub>Mn<sub>1.5</sub>O<sub>4</sub> samples synthesized without and with different molecular weights of PVP

## Electrochemical performance

Figure 5a shows initial charge/discharge curves of  $\text{LiNi}_{0.5}\text{Mn}_{1.5}\text{O}_4$  samples at 0.2 C rate between 3.5 V and 4.95 V. The initial discharge capacities of LNMO, LNMO-PVP<sub>L</sub>, LNMO-PVP<sub>M</sub>, and LNMO-PVP<sub>H</sub> samples are 133.6, 142.7, 138.3, and 136.7 mAh g<sup>-1</sup>, respectively. The higher crystallinity, smaller primary particle size, and homogenous secondary particle distribution lead to the higher discharge capacities of  $\text{LiNi}_{0.5}\text{Mn}_{1.5}\text{O}_4$  samples synthesized with PVP than that without PVP. Compared with LNMO-PVP<sub>M</sub> and LNMO-PVP<sub>H</sub>, the relatively higher initial discharge capacity of LNMO-PVP<sub>L</sub> may be ascribed to its higher Mn<sup>3+</sup> content, since Mn<sup>3+</sup> ions have electrochemical activity while Mn<sup>4+</sup> ions do not. In addition, all samples show two split voltage plateaus at ~4.7 V corresponding to Ni<sup>2+</sup>/Ni<sup>3+</sup> and Ni<sup>3+</sup>/Ni<sup>4+</sup> redox couples, as well as a short voltage plateau at ~4.0 V corresponding to Mn<sup>3+</sup>/Mn<sup>4+</sup> redox couple, manifesting their main *Fd3m* disordered structure. What's more, the length of ~4.0 V plateau can qualitatively estimate the relative Mn<sup>3+</sup> content, calculated by the discharge capacity between 3.8 and 4.25 V divided by the total discharge capacity [32]. Thereby, the calculated Mn<sup>3+</sup> contents are 11.45%, 16.64%, 13.35% and 14.08% for LNMO, LNMO-PVP<sub>L</sub>, LNMO-PVP<sub>M</sub> and LNMO-PVP<sub>H</sub>, respectively, in consistency with above XRD and FT-IR results.

The rate capability curves of  $\text{LiNi}_{0.5}\text{Mn}_{1.5}\text{O}_4$  samples are shown in Fig. 5b, which are tested at rates of 0.2 C, 1 C, 2 C, 5 C, and 10 C (1 C = 147 mA g<sup>-1</sup>), five times at each rate, and then back to 0.2 C. The 0.2 C discharge capacities are almost restored to original values after rate capability test. The discharge capacity of pristine LNMO decreases dramatically to 115.4 mAh g<sup>-1</sup> at 10 C rate, due to low crystallinity, large primary particle size, and severe agglomeration, whereas LNMO-PVP<sub>L</sub>, LNMO-PVP<sub>M</sub>, and LNMO-PVP<sub>H</sub> samples synthesized with PVP exhibit higher discharge capacities of 127.5, 121.4, and 118.8 mAh g<sup>-1</sup> at 10 C rate, respectively. It can be conjectured that the addition of PVP with different molecular weights ameliorates the rate capability of  $\text{LiNi}_{0.5}\text{Mn}_{1.5}\text{O}_4$  material to varying degrees, thanks to higher crystallinity, higher cation disordering degree, smaller primary particle size, and more uniform secondary particle distribution. Among them, LNMO-PVP<sub>L</sub> exhibits the best rate capability, despite with relatively large primary particle size. As previously reported, the rate capability of  $\text{LiNi}_{0.5}\text{Mn}_{1.5}\text{O}_4$  material is more greatly influenced by the surface orientation than by the crystal morphology and size of the material [20]. Compared with other two samples, the presence of {110} surface is more conducive to the diffusion of Li<sup>+</sup> ion, so that LNMO-PVP<sub>L</sub> displays better rate capability. Besides, higher cation disordering degree always means higher electronic conductivity [33], which is also conducive to the rate performance of LNMO-PVP<sub>L</sub> sample. Comparatively, the

relatively poor rate capability of LNMO-PVP<sub>H</sub> sample may be ascribed to lower cation disordering degree, tight bonding between primary particles and absence of {110} exposed surface, in spite of smaller primary particle size.

Figure 5c illustrates the cycling performance curves of all electrodes at 1 C and 25 °C. All electrodes are cycled 3 times at 0.1 C for formation before cycle test. From the figure, we get that the capacity retention rates of LNMO, LNMO-PVP<sub>L</sub>, LNMO-PVP<sub>M</sub>, and LNMO-PVP<sub>H</sub> electrodes after 200 cycles are 82.6%, 92.4%, 90.7%, and 89.8%, respectively; that is, the cycling performance is improved to different extents after the addition of PVP with different molecular weights. As we know, the cycling performance of  $\text{LiNi}_{0.5}\text{Mn}_{1.5}\text{O}_4$  material is mainly determined by the interfacial effects under high voltage [31]. The side reactions on the electrode/electrolyte interface and the continuous formation of CEI (Cathode Electrolyte Interphase) layer mainly account for the capacity degradation of  $\text{LiNi}_{0.5}\text{Mn}_{1.5}\text{O}_4$  material [34]. Compared with LNMO-PVP<sub>L</sub> and LNMO-PVP<sub>M</sub>, the relatively poor cycling performance of LNMO-PVP<sub>H</sub> electrode may be ascribed to smaller primary particle size and more dispersed secondary particles, which increases the contact area between electrode and electrolyte. Correspondingly, the better cycling performance of LNMO-PVP<sub>L</sub> may be attributed to relatively large primary particle size and slightly severe agglomerate structure. Besides, the higher disordering degree is also conducive to the structural stability of LNMO-PVP<sub>L</sub> [4].

The coulombic efficiency curves of all electrodes are also shown in Fig. 5c. The electrolyte decomposition and other side reactions between electrode and electrolyte under high voltage account for the low coulombic efficiencies in initial several cycles [25]. During following cycles,  $\text{LiNi}_{0.5}\text{Mn}_{1.5}\text{O}_4$  materials synthesized with PVP display higher stabilized coulombic efficiencies than pristine one, which suggests that fewer side reactions occur at the electrode/electrolyte interface, resulting in thinner CEI layer on the electrode surface, as ascertained by the following SEM observation in Fig. 8.

To gain insight into the electrochemical characteristics of  $\text{LiNi}_{0.5}\text{Mn}_{1.5}\text{O}_4$  electrodes, CV measurements were carried out at scan rates of 0.10, 0.12, 0.14, 0.16, and 0.18 mV s<sup>-1</sup> in the voltage range of 3.4–5.0 V, respectively, and the obtained curves are shown in Fig. 6a–d. Assuming that the intercalation reaction is controlled by the solid-state diffusion of Li<sup>+</sup> ion, the diffusion coefficient of Li<sup>+</sup> ions ( $D_{\text{Li}}$ ) can be determined based on Randles–Sevcik equation [35]:

$$i_p = (2.69 \times 10^5) n^{3/2} A D_{\text{Li}}^{1/2} \nu^{1/2} C_0 \quad (1)$$

where  $i_p$  is the peak current (A),  $n$  is the number of electrons per reaction species ( $n=1$ ),  $A$  is the surface area of electrode (1.13 cm<sup>2</sup>),  $D_{\text{Li}}$  is the diffusion coefficient of Li<sup>+</sup> ions (cm<sup>2</sup> s<sup>-1</sup>),  $C_0$  is the initial concentration of Li<sup>+</sup> ions in the cathode



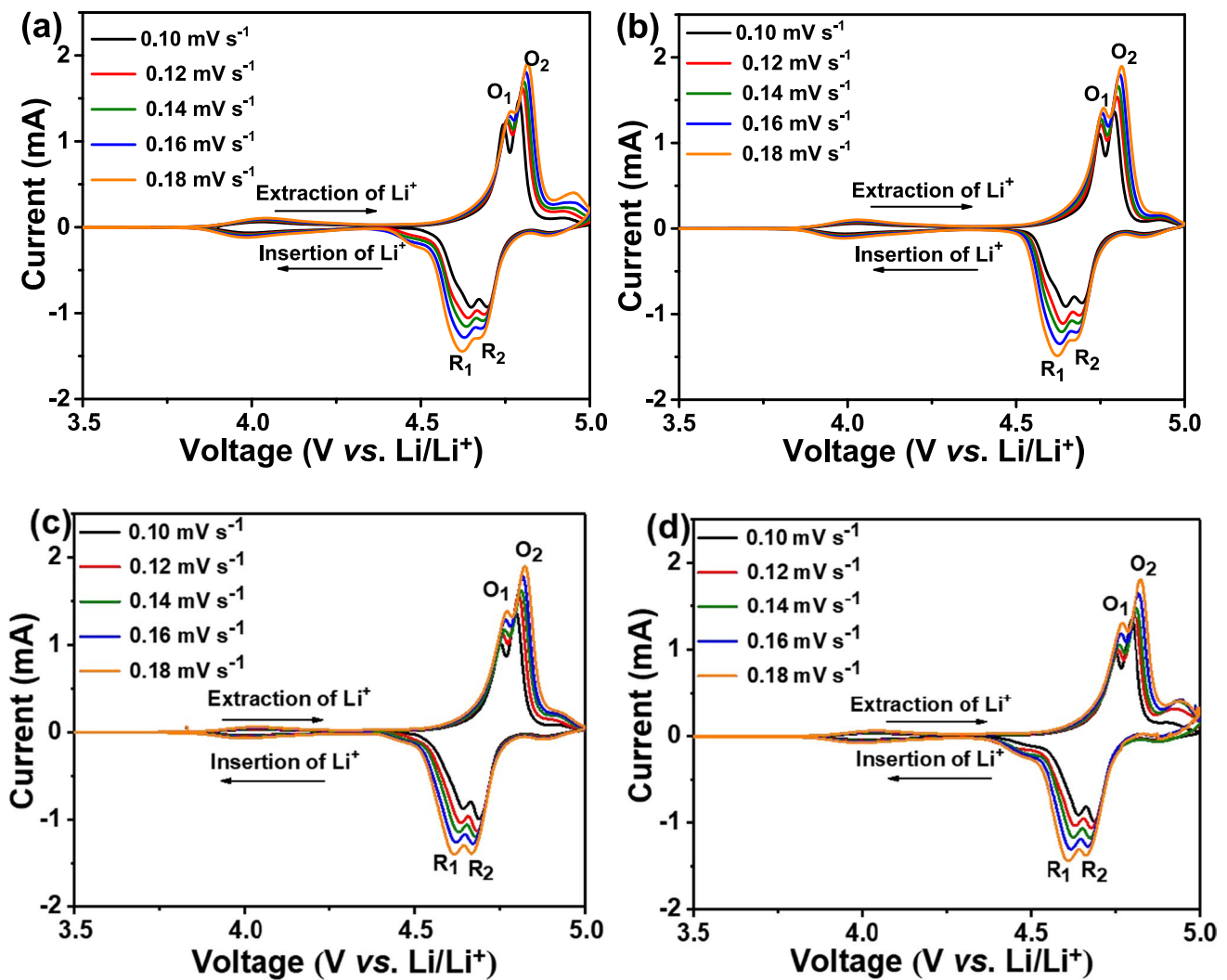


Fig. 6 CV curves obtained at different scan rates for a, e LNMO, b, f LNMO-PVP<sub>L</sub>, c, g LNMO-PVP<sub>M</sub>, and d, h LNMO-PVP<sub>H</sub>

**Table 1** Li<sup>+</sup> ions diffusion coefficients ( $D_{Li}$ ) of LiNi<sub>0.5</sub>Mn<sub>1.5</sub>O<sub>4</sub> samples synthesized without and with different molecular weights of PVP

Sample	$D_{Li} (\times 10^{-9} \text{ cm}^2 \text{ s}^{-1})$				$D_a (\times 10^{-9} \text{ cm}^2 \text{ s}^{-1})$
	O <sub>1</sub>	R <sub>1</sub>	O <sub>2</sub>	R <sub>2</sub>	
LNMO	0.300	0.326	0.274	0.232	0.283
LNMO-PVP <sub>L</sub>	0.143	0.478	0.437	0.288	0.336
LNMO-PVP <sub>M</sub>	0.193	0.404	0.415	0.222	0.308
LNMO-PVP <sub>H</sub>	0.164	0.435	0.357	0.243	0.300

( $C_0 = 8/N_A \cdot V$ ,  $V$  is the unit cell volume obtained by XRD refinement, mol cm<sup>-3</sup>), and  $\nu$  is the scan rate (V s<sup>-1</sup>) [36]. Table 1 lists the calculated  $D_{Li}$  values based on O<sub>1</sub>, R<sub>1</sub>, Q<sub>2</sub>, and R<sub>2</sub> peaks. The average Li<sup>+</sup> ion diffusion coefficients ( $D_a$ ) calculated based on the four  $D_{Li}$  values are  $0.283 \times 10^{-9}$ ,  $0.336 \times 10^{-9}$ ,  $0.308 \times 10^{-9}$ , and  $0.300 \times 10^{-9} \text{ cm}^2 \text{ s}^{-1}$ , respectively, for LNMO, LNMO-PVP<sub>L</sub>, LNMO-PVP<sub>M</sub>, and LNMO-PVP<sub>H</sub>

samples; that is, LNMO-PVP<sub>L</sub> has the highest Li<sup>+</sup> ion diffusion coefficient. It has been reported that Li<sup>+</sup> ion diffusion kinetics depends to a great extent on the crystalline orientation of surface planes in contact with electrolyte, and {110} surfaces possess the most open channels for fast Li<sup>+</sup> ion diffusion due to the alignment of atomic arrangements with Li<sup>+</sup> ion diffusion channel [4, 37]. Compared with LNMO-PVP<sub>M</sub> and LNMO-PVP<sub>H</sub> particles, the presence of extra {110} exposed surfaces is more conducive to the Li<sup>+</sup> ion diffusion of LNMO-PVP<sub>L</sub> particles, thus leading to its better rate capability.

To better elucidate the effect of PVP addition on the cycling performance, EIS measurements were performed on all LiNi<sub>0.5</sub>Mn<sub>1.5</sub>O<sub>4</sub> electrodes after 50, 100, 150, and 200 cycles to observe the impedance change during the cycle. EIS measurement was conducted after the cells were fully discharged to 3.5 V at the given cycle number, followed by letting those at open circuit voltage till reaching the equilibrium, and the obtained Nyquist plots are shown in Fig. 7a–d. It can

be seen that all plots display similar profiles, which consist of two semicircles at high- and middle-frequency region and an inclined line at low-frequency region. The high-frequency and middle-frequency semicircles represent the surface film resistance ( $R_{sf}$ ) and charge transfer resistance ( $R_{ct}$ ), and the

low-frequency inclined line represents a Warburg impedance ( $Z_w$ ). In addition, the high-frequency intercept at the real axis represents a solution resistance ( $R_s$ ) [38]. The plots are fitted by ZView software according to the equivalent circuit in Fig. 7f, and the fitted  $R_{sf}$  values at different cycle numbers

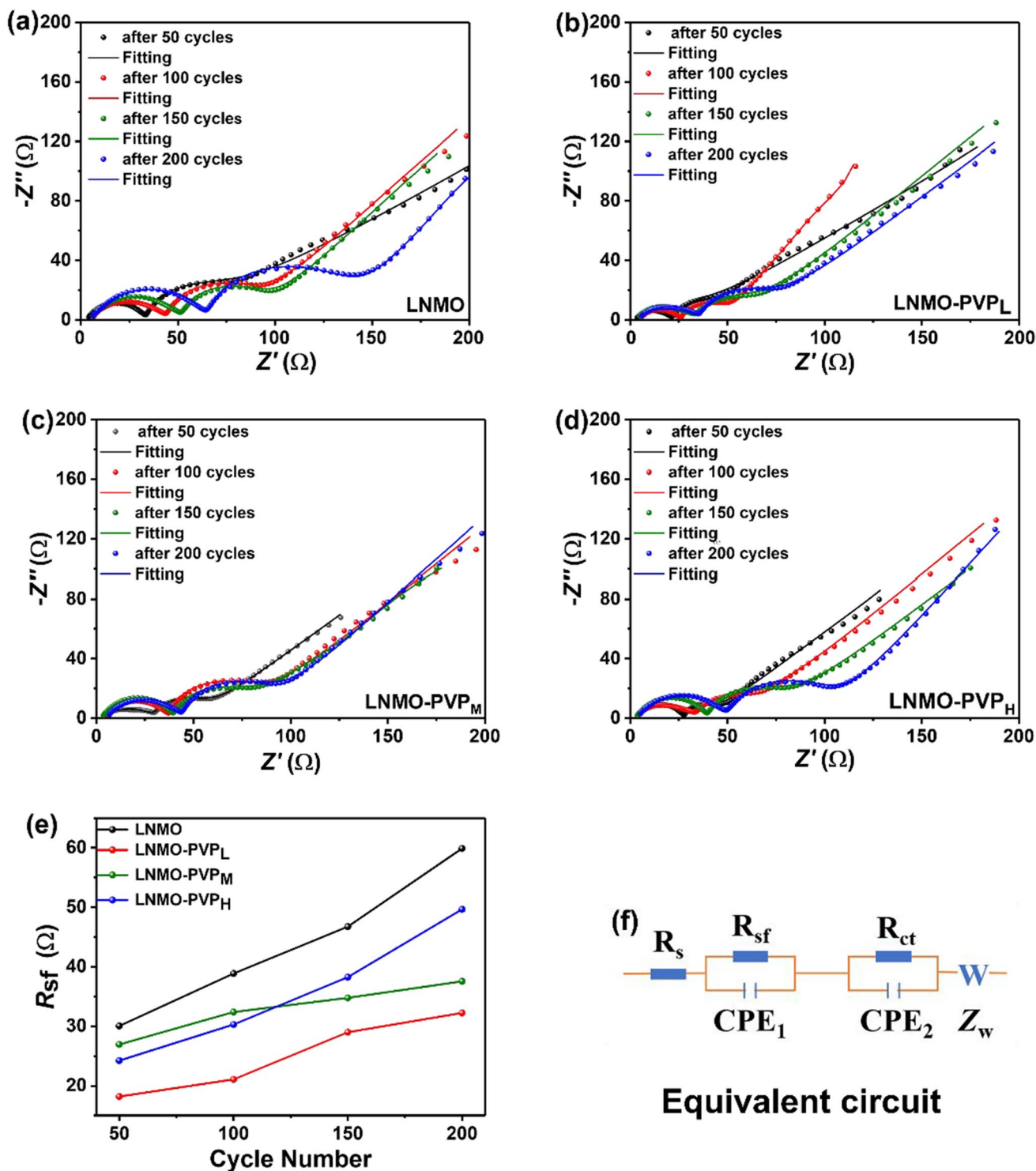
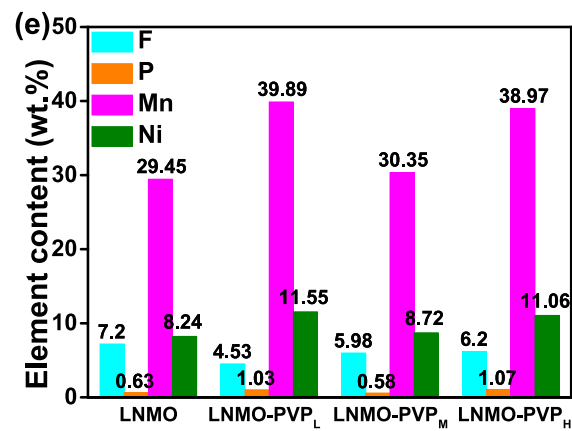
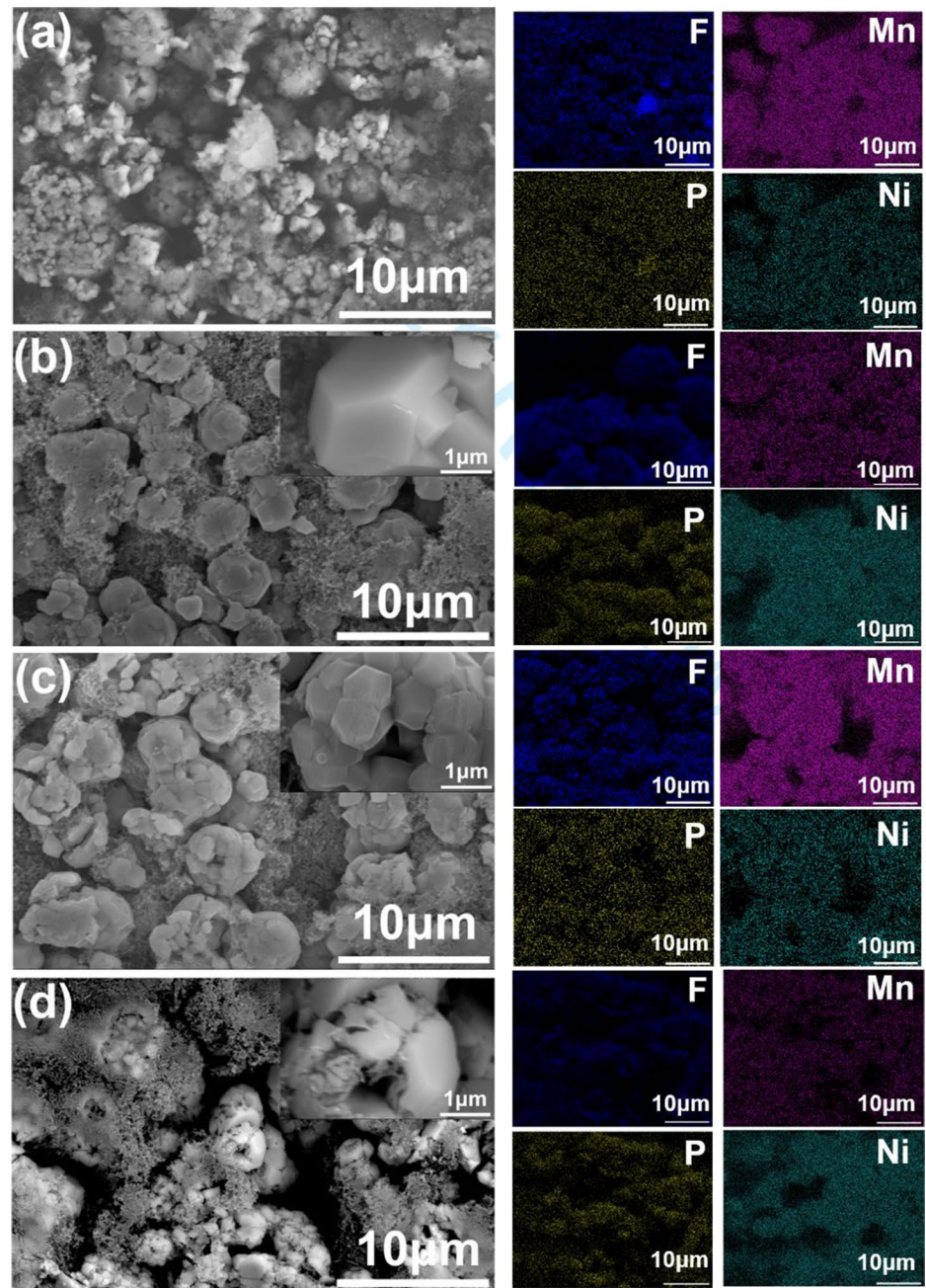


**Fig. 7** Nyquist plots and fitting lines for  $\text{LiNi}_{0.5}\text{Mn}_{1.5}\text{O}_4$  samples synthesized without and with different molecular weights of PVP after different cycles (a–d), variation of  $R_{sf}$  values with cycle number (e), and corresponding equivalent circuit (f)

**Fig. 8** SEM and EDS images for **a** LNMO, **b** LNMO-PVP<sub>L</sub>, **c** LNMO-PVP<sub>M</sub>, **d** LNMO-PVP<sub>H</sub>, and **e** element contents on electrode surface after 200 cycles at 1 C and 25 °C



are illustrated in Fig. 7e. For all electrodes, the gradual increase of  $R_{sf}$  with cycle number means the occurrence of continuous electrolyte decomposition and other side reactions, which leads to the gradual growth of CEI layer during cycling process. Besides, compared with pristine LNMO, the lower  $R_{sf}$  values of PVP-added samples suggests fewer electrolyte decomposition and other side reactions. Among them, LNMO-PVP<sub>L</sub> exhibits the lowest  $R_{sf}$  values during cycling, probably due to the smaller contact area between electrode and electrolyte resulting from the larger primary particle size and slightly severe agglomerate structure, corroborating its optimal cycling performance.

### Post-mortem analysis

The cathodes were disassembled from the cells after 200 cycles and rinsed with DMC and dried overnight in glove box. The SEM images and corresponding EDS images are shown in Fig. 8a–d. In comparison with the collapsed particles of LNMO sample in Fig. 8a, most particles of the samples synthesized with PVP retain their original microsphere structure without collapse, as shown in Fig. 8b–d. From the inset magnified image in Fig. 8b, the cycled LNMO-PVP<sub>L</sub> particle has relatively clean surface, and the truncated octahedral shape is still visible, suggesting the deposition of fewer electrolyte decomposition products, whereas, from the magnified image in the inset of Fig. 8d, more electrolyte decomposition products exist on the surface of LNMO-PVP<sub>H</sub> particle, making the boundary between primary particles blurred. Besides some secondary particles break up, which exposes more fresh surfaces to electrolyte and leads to the occurrence of more interfacial side reactions and consumption of active Li<sup>+</sup> ions, in consistence with its relatively poor cycling performance. The collapse of LNMO-PVP<sub>H</sub> particles may be ascribed to its lower disordering degree. Generally, *Fd3m* space group experiences lower mechanical stress due to one topotactic two-phase transition in comparison with two-step phase transitions between three different cubic phases of *P4<sub>3</sub>2* space group during charge/discharge process [39]. Therefore, lower disordering degree means higher mechanical stress, thus causing the breakage of LNMO-PVP<sub>H</sub> particles.

Figure 8a–d also display the element mapping images of Mn, Ni, F, and P on the electrode surface after 200 cycles, and their corresponding contents are illustrated in Fig. 8e. Obviously, the content of Mn and Ni on the surface of LNMO-PVP<sub>L</sub> electrode is higher than other electrodes, while the content of F element is lower, suggesting the deposition of fewer electrolyte decomposition products and the formation of thinner CEI layer on the surface of LNMO-PVP<sub>L</sub> electrode. This is mainly ascribed to the relatively large primary particle size and slightly severe agglomerate structure, in consistence with its better cycling performance. As well known, F element mainly comes from the decomposition products of LiPF<sub>6</sub> salt, such as LiF, Li<sub>x</sub>PF<sub>y</sub> and Li<sub>x</sub>PO<sub>y</sub>F<sub>z</sub>, which are characteristic of

high resistance. Thereby, the lower F content means lower interfacial resistance, which leads to the better cycling performance of LNMO-PVP<sub>L</sub> electrode. Similarly, the lowest Mn and Ni contents and highest F content match well with the worst cycling performance of pristine LNMO electrode.

### Conclusions

LiNi<sub>0.5</sub>Mn<sub>1.5</sub>O<sub>4</sub> cathode materials with hierarchical microsphere structure have been synthesized via a combined coprecipitation-hydrothermal method under the assistance of PVP with different molecular weights (average Mw: 10,000/58,000/1,300,000) followed by high-temperature calcination. XRD and FT-IR results show that the addition of PVP with different molecular weights does not change the *Fd3m* disordered structure, but increases the crystallinity degree and cation disordering degree of LiNi<sub>0.5</sub>Mn<sub>1.5</sub>O<sub>4</sub> material. SEM observation shows that the three materials synthesized with PVP exhibit hierarchical microsphere structure composed of truncated octahedral primary particles. It should be noteworthy that the primary particle size, shape, and secondary particle distribution are greatly influenced by the molecular weights of PVP. The increase of PVP molecular weight leads to the decreasing primary particle size and more uniform secondary particle distribution. Besides, compared with LNMO-PVP<sub>M</sub> (average Mw: 58,000) and LNMO-PVP<sub>H</sub> (average Mw: 1,300,000) particles, LNMO-PVP<sub>L</sub> (average Mw: 10,000) particle exhibits extra {110} surface besides {111} and {100} surfaces. Among them, LNMO-PVP<sub>L</sub> material exhibits the optimal rate capability (127.5 mAh g<sup>-1</sup> at 10 C), mainly due to higher cation disordering degree and extra exposed {110} surface. LNMO-PVP<sub>L</sub> sample also exhibits better cycling performance with capacity retention rate of 92.4% after 200 cycles at 1 C and 25 °C, thanks to the relatively large primary particle size and slightly severe agglomerate structure. Post-mortem analysis reveals that the addition of PVP with different molecular weights could effectively reduce the side reactions on electrode/electrolyte interface, resulting in the formation of thinner CEI layer and then the improved cycling performance of LiNi<sub>0.5</sub>Mn<sub>1.5</sub>O<sub>4</sub> material.

**Funding** This work was supported by the National Natural Science Foundation of China (grant number 51802074).

### References

1. Liang W, Wang P, Ding H, Wang B, Li S (2021) Granularity control enables high stability and elevated-temperature properties of micron-sized single-crystal LiNi<sub>0.5</sub>Mn<sub>1.5</sub>O<sub>4</sub> cathodes at high voltage. *J Materiomics* 7:1049–1060. <https://doi.org/10.1016/j.jmat.2021.02.003>

2. Yi T-F, Mei J, Zhu Y-R (2016) Key strategies for enhancing the cycling stability and rate capacity of  $\text{LiNi}_{0.5}\text{Mn}_{1.5}\text{O}_4$  as high-voltage cathode materials for high power lithium-ion batteries. *J Power Sources* 316:85–105. <https://doi.org/10.1016/j.jpowsour.2016.03.070>
3. Kim JH, Pieczonka NPW, Yang L (2014) Challenges and approaches for high-voltage spinel lithium-ion batteries. *ChemPhysChem* 15:1940–1954. <https://doi.org/10.1002/cphc.201400052>
4. Yu X, Yu WA, Manthiram A (2021) Advances and prospects of high-voltage spinel cathodes for lithium-based batteries. *Small Methods* 5:2001196. <https://doi.org/10.1002/smt.202001196>
5. Feng S, Kong X, Sun H, Wang B, Luo T, Liu G (2018) Effect of Zr doping on  $\text{LiNi}_{0.5}\text{Mn}_{1.5}\text{O}_4$  with ordered or disordered structures. *J Alloys Compd* 749:1009–1018. <https://doi.org/10.1016/j.jallcom.2018.03.177>
6. Xu R, Zhang X, Chamoun R, Shui J, Li JCM, Lu J, Amine K, Belharouak I (2015) Enhanced rate performance of  $\text{LiNi}_{0.5}\text{Mn}_{1.5}\text{O}_4$  fibers synthesized by electrospinning. *Nano Energy* 15:616–624. <https://doi.org/10.1016/j.nanoen.2015.05.023>
7. Chen Z, Zhao R, Du P, Hu H, Wang T, Zhu L, Chen H (2014) Polyhedral  $\text{LiNi}_{0.5}\text{Mn}_{1.5}\text{O}_4$  with excellent electrochemical properties for lithium-ion batteries. *J Mater Chem A* 2:12835–12848. <https://doi.org/10.1039/C4TA02371D>
8. Yan Z, Cai S, Zhou X, Zhao Y, Miao L (2012) Sol-gel synthesis of nanostructured  $\text{Li}_2\text{FeSiO}_4/\text{C}$  as cathode material for lithium ion battery. *J Electrochem Soc* 159:A894–A898. <https://doi.org/10.1149/2.110206jes>
9. Lin HB, Zhang YM, Hu JN, Wang YT, Xing LD, Xu MQ, Li XP, Li WS (2014)  $\text{LiNi}_{0.5}\text{Mn}_{1.5}\text{O}_4$  nanoparticles: synthesis with synergistic effect of polyvinylpyrrolidone and ethylene glycol and performance as cathode of lithium ion battery. *J Power Sources* 257:37–44. <https://doi.org/10.1016/j.jpowsour.2014.01.089>
10. Zhang X, Cheng F, Zhang K, Liang Y, Yang S, Liang J, Chen J (2012) Facile polymer-assisted synthesis of  $\text{LiNi}_{0.5}\text{Mn}_{1.5}\text{O}_4$  with a hierarchical micro-nano structure and high rate capability. *RSC Adv* 2:5669–5675. <https://doi.org/10.1039/C2RA20669B>
11. Mao J, Dai K, Zhai Y (2012) Electrochemical studies of spinel  $\text{LiNi}_{0.5}\text{Mn}_{1.5}\text{O}_4$  cathodes with different particle morphologies. *Electrochim Acta* 63:381–390. <https://doi.org/10.1016/j.electacta.2011.12.129>
12. Zhou H, Yang Z, Yin C, Yang S, Li J (2018) Fabrication of nanoplate Li-rich cathode material via surfactant-assisted hydrothermal method for lithium-ion batteries. *Ceram Int* 44:20514–20523. <https://doi.org/10.1016/j.ceramint.2018.08.048>
13. Tian Y, Chen M, Xue S, Cai Y, Huang Q, Liu X, Li W (2018) Template-determined microstructure and electrochemical performances of Li-rich layered metal oxide cathode. *J Power Sources* 401:343–353. <https://doi.org/10.1016/j.jpowsour.2018.09.010>
14. Xiang X, Li X, Li W (2013) Preparation and characterization of size-uniform  $\text{Li}[\text{Li}_{0.131}\text{Ni}_{0.304}\text{Mn}_{0.565}]\text{O}_2$  particles as cathode materials for high energy lithium ion battery. *J Power Sources* 230:89–95. <https://doi.org/10.1016/j.jpowsour.2012.12.050>
15. Koczkur KM, Mourdikoudis S, Polavarapu L, Skrabalak SE (2015) Polyvinylpyrrolidone (PVP) in nanoparticle synthesis. *Dalton Trans* 44:17883–17905. <https://doi.org/10.1039/C5DT02964C>
16. Tao F, X-x Yan J-J, Liu H-L Zhang, Chen L (2016) Effects of PVP-assisted  $\text{Co}_3\text{O}_4$  coating on the electrochemical and storage properties of  $\text{LiNi}_{0.6}\text{Co}_{0.2}\text{Mn}_{0.2}\text{O}_2$  at high cut-off voltage. *Electrochim Acta* 210:548–556. <https://doi.org/10.1016/j.electacta.2016.05.060>
17. Qian R, Yao M, Xiao F, Yao T, Lu H, Liu Y, Shi J-W, Cheng Y, Wang H (2022) Polyvinylpyrrolidone regulated synthesis of mesoporous titanium niobium oxide as high-performance anode for lithium-ion batteries. *J Colloid Interface Sci* 608:1782–1791. <https://doi.org/10.1016/j.jcis.2021.10.073>
18. Liu D, Zhu W, Trottier J, Gagnon C, Barray F, Guerfi A, Mauger A, Groult H, Julien CM, Goodenough JB, Zaghib K (2014) Spinel materials for high-voltage cathodes in Li-ion batteries. *RSC Adv* 4:154–167. <https://doi.org/10.1039/C3RA45706K>
19. Xue Y, Wang Z, Zheng L, Yu F, Liu B, Zhang Y, Ke K (2015) Investigation on preparation and performance of spinel  $\text{LiNi}_{0.5}\text{Mn}_{1.5}\text{O}_4$  with different microstructures for lithium-ion batteries. *Sci Rep* 5:13299. <https://doi.org/10.1038/srep13299>
20. Yin C, Zhou H, Yang Z, Li J (2018) Synthesis and electrochemical properties of  $\text{LiNi}_{0.5}\text{Mn}_{1.5}\text{O}_4$  for Li-ion batteries by the metal-organic framework method. *ACS Appl Mater Interfaces* 10:13625–13634. <https://doi.org/10.1021/acsami.8b02553>
21. Lan L, Li S, Li J, Lu L, Lu Y, Huang S, Xu S, Pan C, Zhao F (2018) Enhancement of the electrochemical performance of the spinel structure  $\text{LiNi}_{0.5-x}\text{Ga}_x\text{Mn}_{1.5}\text{O}_4$  cathode material by Ga doping. *Nanoscale Res Lett* 13:251. <https://doi.org/10.1186/s11671-018-2666-3>
22. Kunduraci M, Al-Sharab JF, Amatucci GG (2006) High-power nanostructured  $\text{LiMn}_{2-x}\text{Ni}_x\text{O}_4$  high-voltage lithium-ion battery electrode materials: electrochemical impact of electronic conductivity and morphology. *Chem Mater* 18:3585–3592. <https://doi.org/10.1021/cm060729s>
23. Kunduraci M, Amatucci GG (2006) Synthesis and characterization of nanostructured 4.7 V  $\text{Li}_x\text{Mn}_{1.5}\text{Ni}_{0.5}\text{O}_4$  spinels for high-power lithium-ion batteries. *J Electrochem Soc* 153:A1345–A1352. <https://doi.org/10.1149/1.2198110>
24. Zheng X, Liu W, Qu Q, Zheng H, Huang Y (2019) Bi-functions of titanium and lanthanum co-doping to enhance the electrochemical performance of spinel  $\text{LiNi}_{0.5}\text{Mn}_{1.5}\text{O}_4$  cathode. *J Materiomics* 5:156–163. <https://doi.org/10.1016/j.jmat.2019.01.007>
25. Manthiram A, Chemelewski K, Lee E-S (2014) A perspective on the high-voltage  $\text{LiMn}_{1.5}\text{Ni}_{0.5}\text{O}_4$  spinel cathode for lithium-ion batteries. *Energy Environ Sci* 7:1339–1350. <https://doi.org/10.1039/C3EE42981D>
26. Sun Y-H, Dong P-P, Liu S, Nan J-M (2016) Influence of surfactants on the microstructure and electrochemical performance of the tin oxide anode in lithium ion batteries. *Mater Res Bull* 74:299–310. <https://doi.org/10.1016/j.materresbull.2015.10.050>
27. Patel V, Dharaiya N, Ray D, Aswal VK, Bahadur P (2014) pH controlled size/shape in CTAB micelles with solubilized polar additives: a viscometry, scattering and spectral evaluation. *Colloids Surf A* 455:67–75. <https://doi.org/10.1016/j.colsurfa.2014.04.025>
28. Izu N, Uchida T, Matsubara I, Itoh T, Shin W, Nishibori M (2011) Formation mechanism of monodispersed spherical core-shell ceria/polymer hybrid nanoparticles. *Mater Res Bull* 46:1168–1176. <https://doi.org/10.1016/j.materresbull.2011.04.019>
29. Kim J-S, Kim KS, Cho W, Shin WH, Kanno R, Choi JW (2012) A truncated manganese spinel cathode for excellent power and lifetime in lithium-ion batteries. *Nano Lett* 12:6358–6365. <https://doi.org/10.1021/nl303619s>
30. Yan J, Wang J, Liu H, Bakenov Z, Gosselink D, Chen P (2012) Rechargeable hybrid aqueous batteries. *J Power Sources* 216:222–226. <https://doi.org/10.1016/j.jpowsour.2012.05.063>
31. Liu H, Wang J, Zhang X, Zhou D, Qi X, Qiu B, Fang J, Kloepsch R, Schumacher G, Liu Z, Li J (2016) Morphological evolution of high-voltage spinel  $\text{LiNi}_{0.5}\text{Mn}_{1.5}\text{O}_4$  cathode materials for lithium-ion batteries: the critical effects of surface orientations and particle size. *ACS Appl Mater Interfaces* 8:4661–4675. <https://doi.org/10.1021/acsami.5b11389>
32. Zeng Y-P, X-I Wu, Mei P, Cong L-N, Yao C, Wang R-S, Xie H-M, Sun L-Q (2014) Effect of cationic and anionic substitutions on the electrochemical properties of  $\text{LiNi}_{0.5}\text{Mn}_{1.5}\text{O}_4$  spinel cathode materials. *Electrochim Acta* 138:493–500. <https://doi.org/10.1016/j.electacta.2014.06.082>

33. Chen Z, Wang X, Tian X, Zhong H, Hu C, Wen J, Peng Y, Xu J, Wu C (2019) Synthesis of ordered  $\text{LiNi}_{0.5}\text{Mn}_{1.5}\text{O}_4$  nanoplates with exposed 100 and 110 crystal planes and its electrochemical performance for lithium ions batteries. *Solid State Ionics* 333:50–56. <https://doi.org/10.1016/j.ssi.2019.01.022>
34. Cui X, Geng T, Zhang F, Zhang N, Zhao D, Li C, Li S (2020) The influence of the voltage plateau on the coulombic efficiency and capacity degradation in  $\text{LiNi}_{0.5}\text{Mn}_{1.5}\text{O}_4$  materials. *J Alloys Compd* 820:153443. <https://doi.org/10.1016/j.jallcom.2019.153443>
35. Mukherjee R, Krishnan R, Lu T-M, Koratkar N (2012) Nanostructured electrodes for high-power lithium ion batteries. *Nano Energy* 1:518–533. <https://doi.org/10.1016/j.nanoen.2012.04.001>
36. Liu H, Li M, Xiang M, Guo J, Bai H, Bai W, Liu X (2021) Effects of crystal structure and plane orientation on lithium and nickel co-doped spinel lithium manganese oxide for long cycle life lithium-ion batteries. *J Colloid Interface Sci* 585:729–739. <https://doi.org/10.1016/j.jcis.2020.10.052>
37. Gong J, Yan S, Lang Y, Zhang Y, Fu S, Guo J, Wang L, Liang G (2021) Effect of  $\text{Cr}^{3+}$  doping on morphology evolution and electrochemical performance of  $\text{LiNi}_{0.5}\text{Mn}_{1.5}\text{O}_4$  material for Li-ion battery. *J Alloys Compd.* 859:157885. <https://doi.org/10.1016/j.jallcom.2020.157885>
38. Yi T, Shi L, Han X, Wang F, Zhu Y, Xie Y (2021) Approaching high-performance lithium storage materials by constructing hierarchical  $\text{CoNiO}_2@ \text{CeO}_2$  nanosheets. *Energy Environ Mater* 4:586–595. <https://doi.org/10.1002/eem2.12140>
39. Kim J-H, Myung S-T, Yoon CS, Kang SG, Sun Y-K (2004) Comparative study of  $\text{LiNi}_{0.5}\text{Mn}_{1.5}\text{O}_{4-\delta}$  and  $\text{LiNi}_{0.5}\text{Mn}_{1.5}\text{O}_4$  cathodes having two crystallographic structures:  $\text{Fd}3\text{m}$  and  $\text{P}4332$ . *Chem Mater* 16:906–914. <https://doi.org/10.1021/cm035050s>

**Publisher's note** Springer Nature remains neutral with regard to jurisdictional claims in published maps and institutional affiliations.

Springer Nature or its licensor holds exclusive rights to this article under a publishing agreement with the author(s) or other rightsholder(s); author self-archiving of the accepted manuscript version of this article is solely governed by the terms of such publishing agreement and applicable law.